


A free-standing lithium phosphorus oxynitride thin film electrolyte promotes uniformly dense lithium metal deposition with no external pressure

Received: 12 July 2022

Accepted: 4 July 2023

Published online: 03 August 2023

 Check for updates

Diyi Cheng¹, Thomas Wynn¹, Bingyu Lu², Maxwell Marple³, Bing Han², Ryosuke Shimizu², Bhagath Sreenarayanan², Jeffery Bickel⁴, Peter Hosemann⁴, Yangyuchen Yang¹, Han Nguyen², Weikang Li², Guomin Zhu², Minghao Zhang²✉ & Ying Shirley Meng^{1,2,5}✉

Lithium phosphorus oxynitride (LiPON) is an amorphous solid electrolyte that has been extensively studied over the last three decades. Despite the promise of pairing it with various electrode materials, LiPON's rigidity and air sensitivity set limitations to understanding its intrinsic properties. Here we report a methodology to synthesize LiPON in a free-standing form that manifests remarkable flexibility and a Young's modulus of ~33 GPa. We use solid-state nuclear magnetic resonance and differential scanning calorimetry to quantitatively reveal the chemistry of the Li/LiPON interface and the presence of a well-defined LiPON glass-transition temperature of 207 °C. Combining interfacial stress and a gold seeding layer, our free-standing LiPON shows a uniformly dense deposition of lithium metal without the aid of external pressure. This free-standing LiPON film offers opportunities to study fundamental properties of LiPON for interface engineering for solid-state batteries.

One of the long-lasting debates on the fundamental understanding of lithium phosphorus oxynitride (LiPON) material pertains to the nitrogen-bonding structure and its impact on lithium transport properties. Early studies on the chemistry of LiPON primarily relied on X-ray photoelectron spectroscopy (XPS), where peak assignments have been disputed based on different hypotheses^{1,2,3}. Alternative methods suitable for probing the local bonding environment, such as the neutron paired distribution function and solid-state nuclear magnetic resonance (ss-NMR), have previously been unable to validate existing hypotheses due to the difficulty of obtaining a high enough signal-to-noise (S/N) ratio in the presence of the LiPON's substrate.

Nevertheless, Lacivita et al. managed to obtain sufficient sample for neutron paired distribution function measurements by scraping LiPON from the substrate³. Another aspect of LiPON research lies at its interfaces with various electrode materials. Despite some recent knowledge gained on LiPON-associated interfaces^{4–8}, the electrochemomechanical properties of such interfaces appear not to have been explored, although these could serve as critical metrics determining mechanical behaviours at the interface that affect battery cycling⁹. Nevertheless, due to the presence of substrates, the limited methodologies for studying the mechanical properties of LiPON have also created some ambiguity in literature^{10,11}.

¹Materials Science and Engineering Program, University of California San Diego, La Jolla, CA, USA. ²Department of NanoEngineering, University of California San Diego, La Jolla, CA, USA. ³Physical and Life Science Directorate, Lawrence Livermore National Laboratory, Livermore, CA, USA. ⁴Nuclear Engineering Department, University of California Berkeley, Berkeley, CA, USA. ⁵Pritzker School of Molecular Engineering, University of Chicago, Chicago, IL, USA. ✉e-mail: miz016@eng.ucsd.edu; shirleymeng@uchicago.edu

The dilemma associated with the substrate and the lack of active material for measurements originates from the conventional synthesis methods of LiPON thin films. In fact, a variety of methods are available to synthesize LiPON besides radiofrequency (RF) sputtering^{2,12–19} (Extended Data Table 1). Methods that get around the use of substrate, such as ammonolysis, plasma synthesis or ball milling, suffer from either altered LiPON properties or the introduction of interfacial impedance between LiPON particles^{17–19}.

In this work, we introduce a different methodology to synthesize a LiPON thin film that is in free-standing form without a rigid solid substrate. By leveraging the form factor of this flexible free-standing LiPON (FS-LiPON) thin film, fundamental insights have been obtained from characterization by ss-NMR, differential scanning calorimetry (DSC) and nanoindentation. With the presence of interfacial stress at the Cu/FS-LiPON interface and the introduction of a gold seeding layer, we further demonstrate electrochemical deposition of uniform and fully dense lithium metal under zero external pressure, which provides fresh perspectives on interface engineering in bulk lithium metal solid-state batteries.

A flexible FS-LiPON thin film

Figure 1a depicts the fabrication procedure of FS-LiPON. Before undertaking RF sputtering, a spin-coating method was used to coat a clean glass substrate with photoresist. Details of the spin-coating procedure can be found in Methods. LiPON thin film was then deposited onto the coated glass substrate by RF sputtering under N₂ plasma. After RF sputtering, the LiPON sample was transferred into a container filled with dimethyl carbonate (DMC) solvent in an argon-filled glovebox. The substrate and LiPON film were fully immersed in DMC overnight. Photoresist was then dissolved by DMC, after which LiPON film delaminated from the glass substrate and was ready for pick-up. Unlike the usual way of producing LiPON thin film on a solid substrate, this method yields LiPON film in a free-standing form that exhibits transparency and remarkable flexibility as shown in Fig. 1b and Supplementary Video 1. Depending on the substrate size, deposition area and deposition time, the area, thickness and sample amount of FS-LiPON can be controlled with this procedure (Extended Data Fig. 1).

We performed a variety of characterizations to ensure that the structure, chemical bonding environments and electrical properties of FS-LiPON are not affected during the above synthesis procedure. Cross-sectional scanning electron microscopy (SEM) and energy-dispersive X-ray spectroscopy (EDS) elemental mapping (Extended Data Fig. 2) demonstrate that FS-LiPON retains its fully dense nature in this 3.7- μm -thick film and that phosphorus, oxygen and nitrogen are uniformly distributed across the sample. The X-ray diffraction results (Extended Data Fig. 3a) indicate the amorphous characteristic of FS-LiPON. Figure 1c shows the XPS results of FS-LiPON thin film; the O 1s, N 1s, P 2p and Li 1s regions manifest features consistent with substrate-based LiPON (Sub-LiPON) as shown in Extended Data Figs. 4 and 5 and reported in the literature^{20,21}. EDS elemental mapping (Extended Data Fig. 3b) also confirms that nitrogen, phosphorus and oxygen are uniformly distributed on the surface of the FS-LiPON film. In its role as a solid-state electrolyte (SSE), LiPON acts as an ionic conductor while also being an excellent electrical insulator. Electrochemical impedance spectroscopy (EIS) and d.c. polarization were subsequently used to examine the electrical properties of FS-LiPON. The EIS spectrum in Fig. 1d yields an ionic conductivity of $2.5 \times 10^{-6} \text{ S cm}^{-1}$ for FS-LiPON, consistent with that of Sub-LiPON shown in Extended Data Fig. 6. The d.c. polarization plot in Fig. 1e gives an electronic conductivity of $1.2 \times 10^{-14} \text{ S cm}^{-1}$, on the order of that of Sub-LiPON reported in the literature^{20,22}. Therefore, despite its free-standing form, FS-LiPON exhibits properties consistent with those of Sub-LiPON.

Further exploration of the fundamentals of LiPON

The Li/LiPON interface remains one of the most important interfaces in the solid-state battery field and shows extraordinary

electrochemical stability^{7,23}. As a model example to demonstrate the advantage of using FS-LiPON for spectroscopic characterization, ss-NMR was performed on an Li/FS-LiPON sample and the results are shown in Fig. 2a–c. The Li/FS-LiPON sample was prepared by depositing lithium metal on FS-LiPON film by thermal evaporation. Figure 2a shows the ³¹P magic angle spinning (MAS) NMR spectra of FS-LiPON and Li/FS-LiPON. A high S/N ratio of the NMR spectra was obtained, attributed to the increased sampling volume permitted by the free-standing form of the samples. Based on previous assignments for FS-LiPON²⁴, four different structural units are identified in each spectrum, including orthophosphate tetrahedra PO₄³⁻ (Q_0^0), P₂O₇⁴⁻ dimers (Q_0^1), bridging-nitrogen P₂O₆N⁵⁻ dimers (Q_1^1) and apical-nitrogen PO₃N⁴⁻ units (Q_1^0). A clear difference regarding the content of these structural units is shown in Fig. 2b. The Li/FS-LiPON sample shows an increase (13%) of Q_0^0 units relative to the FS-LiPON sample at the expense of PON units (Q_1^0 and Q_1^1). This increase in PO₄³⁻ content indicates that a large amount of Li₃PO₄ components were generated between lithium metal and LiPON as a result of interface formation, consistent with our previous observation via cryogenic electron microscopy⁷. The decrease in the other structural units such as bridging-oxygen configuration (Q_0^1), bridging-nitrogen configuration (Q_1^1) and apical-nitrogen configuration (Q_1^0) in turn facilitate the formation of interface components such as Li₃N and Li₂O. The ⁷Li MAS NMR spectrum of Li/FS-LiPON in Fig. 2c shows a clear shoulder around 7.5 ppm compared with FS-LiPON, indicating Li₃N formation at the interface²⁵. The slight peak shift shown in Fig. 2c may be due to dynamic heterogeneities between the interfacial lithium ions and lithium ions deep in LiPON. A lithium metal signal was also clearly observed at 264 ppm (Extended Data Fig. 7). Previous electron microscopy observations probed the spatial distribution of interface components between lithium metal and LiPON^{7,8}, while the above ss-NMR results of the Li/FS-LiPON sample provide quantitative insights on the content of the interface components, revealing the amount of Li₃N and Li₃PO₄ formation as the interface products. The coupling of ss-NMR results with cryogenic electron microscopy observation give a more complete view of the Li/LiPON interface both compositionally and spatially.

The nature of FS-LiPON also enables analysis of its thermal properties. LiPON is known to be a glassy material and the glass-transition temperature is one of the most important metrics to determine the metastable states and application environments of such materials. Nevertheless, limited by the insufficient amount of active material for measurement, previously documented trials using DSC to examine the glass-transition temperature of Sub-LiPON failed to capture clear transition behaviours²⁶. In an attempt to compensate for this, DSC was conducted on FS-LiPON. The results in Fig. 2d show an obvious glass transition with an onset temperature of 207 °C and an inflection around 234 °C, consistent with the LiPON glass-transition temperature measured by spectroscopic ellipsometry²⁷. Subsequent thermal response further captured the crystallization process of LiPON, along with the gas evolution observed during heating (inset images in Fig. 2d). DSC results suggest that LiPON should be handled at temperatures <325 °C. Extra consideration needs to be taken when heat treatment is performed on LiPON-related samples/devices.

Another intriguing finding lies in LiPON's mechanical properties. Note that it is essential to maintain an inert environment during the mechanical examination of LiPON: Extended Data Fig. 8 and Supplementary Video 2 show that FS-LiPON stiffened due to air exposure after 3 days. Figure 2e displays the nanoindentation results collected within a vacuum chamber. The hardness values were plotted against contact depth of the indenter into FS-LiPON from continuous-stiffness measurement (CSM), with statistics collected from over 100 indentation locations (Fig. 2e, inset, shows the indent array at one sampling region). Nanoindentation gives an average hardness value of $\sim 2.7 \text{ GPa}$ for FS-LiPON in the displacement range from 60 nm to 200 nm. Hardness values below 60 nm were primarily a surface effect and have

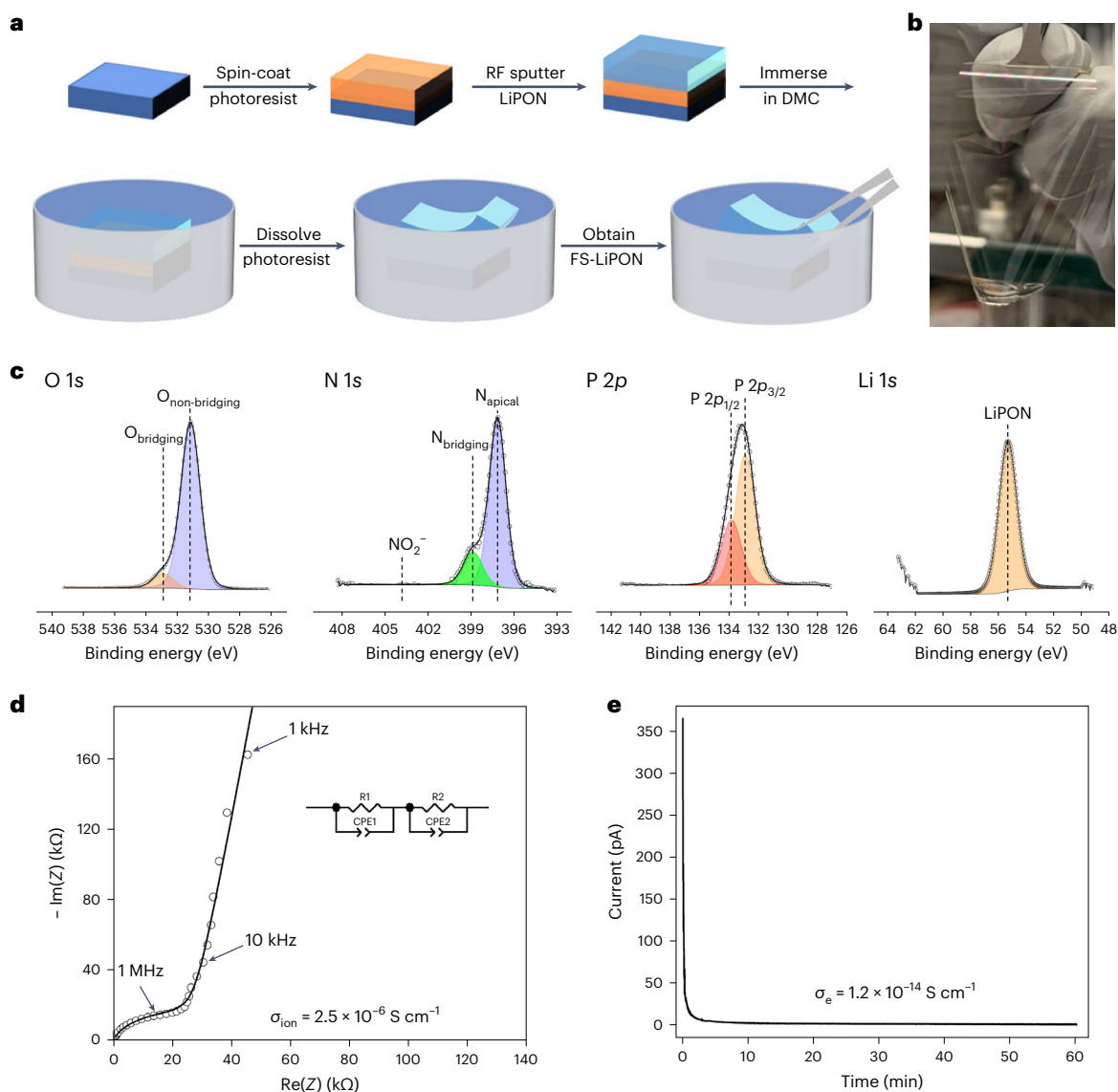


Fig. 1 Synthesis procedure and basic properties of FS-LiPON. **a**, Schematic of the synthesis procedure for FS-LiPON. **b**, Photograph of a transparent and flexible FS-LiPON thin film. **c**, XPS spectra of the O 1s, N 1s, P 2p and Li 1s regions of the FS-LiPON thin film. **d**, EIS plot of FS-LiPON. The equivalent circuit is

shown as an inset, where R1 is the ionic resistance of FS-LiPON film and CPE1 is the dielectric polarization capacitance of FS-LiPON film. R2 and CPE2 are the resistance and capacitance generated by potential interfaces between copper and FS-LiPON at medium frequency. **e**, Direct current polarization of FS-LiPON.

been excluded when determining the film hardness. This hardness of FS-LiPON is lower than the previously reported value of 3.9 GPa on Sub-LiPON²⁸. Based on the mathematical methods developed by Ma et al.²⁹ to determine the Young's modulus from hardness, we obtained an average Young's modulus of FS-LiPON of ~33 GPa, in contrast to the previously reported value of ~80 GPa for Sub-LiPON²⁸. It has been documented that the vacuum deposition process commonly generates residual stress within thin films because the substrate may experience thermal expansion, contraction or lattice mismatch, etc., during the deposition³⁰. Specifically, the sputtering process tends to generate compressive residual stress in deposited thin films, which can affect their mechanical properties, resulting in, for example, increased hardness and Young's modulus³¹. Therefore, the removal of substrate from FS-LiPON potentially releases stress within the LiPON film, leading to the observed diminished hardness and Young's modulus. This observation also suggests the importance of quantifying residual stress in LiPON film before determining its mechanical properties. A series of bending tests that explore LiPON's flexibility with regard to film

thickness are summarized in Supplementary Video 3 and Extended Data Fig. 9.

The above results again illustrate the potential for using this free-standing film to obtain the native properties of LiPON material itself. Regarding the mechanical properties, further tests such as tensile testing, compression testing, etc., can be performed on FS-LiPON, which would otherwise be impossible to conduct on Sub-LiPON.

Electrochemical activity of FS-LiPON

Apart from its intrinsic properties, FS-LiPON is also demonstrated to be applicable in electrochemical devices. An FS-LiPON Li-Cu cell was fabricated using the configuration shown in Fig. 3a, where copper and lithium electrodes with the same designed area were aligned across the FS-LiPON film. The as-fabricated Li-Cu cell harnesses the flexible nature of FS-LiPON as shown in Fig. 3b. The flexibility of the cell is further demonstrated in Fig. 3c, which shows how the cell can be bent by tweezers while still able to sustain lithium metal plating and stripping capability afterwards. After cell

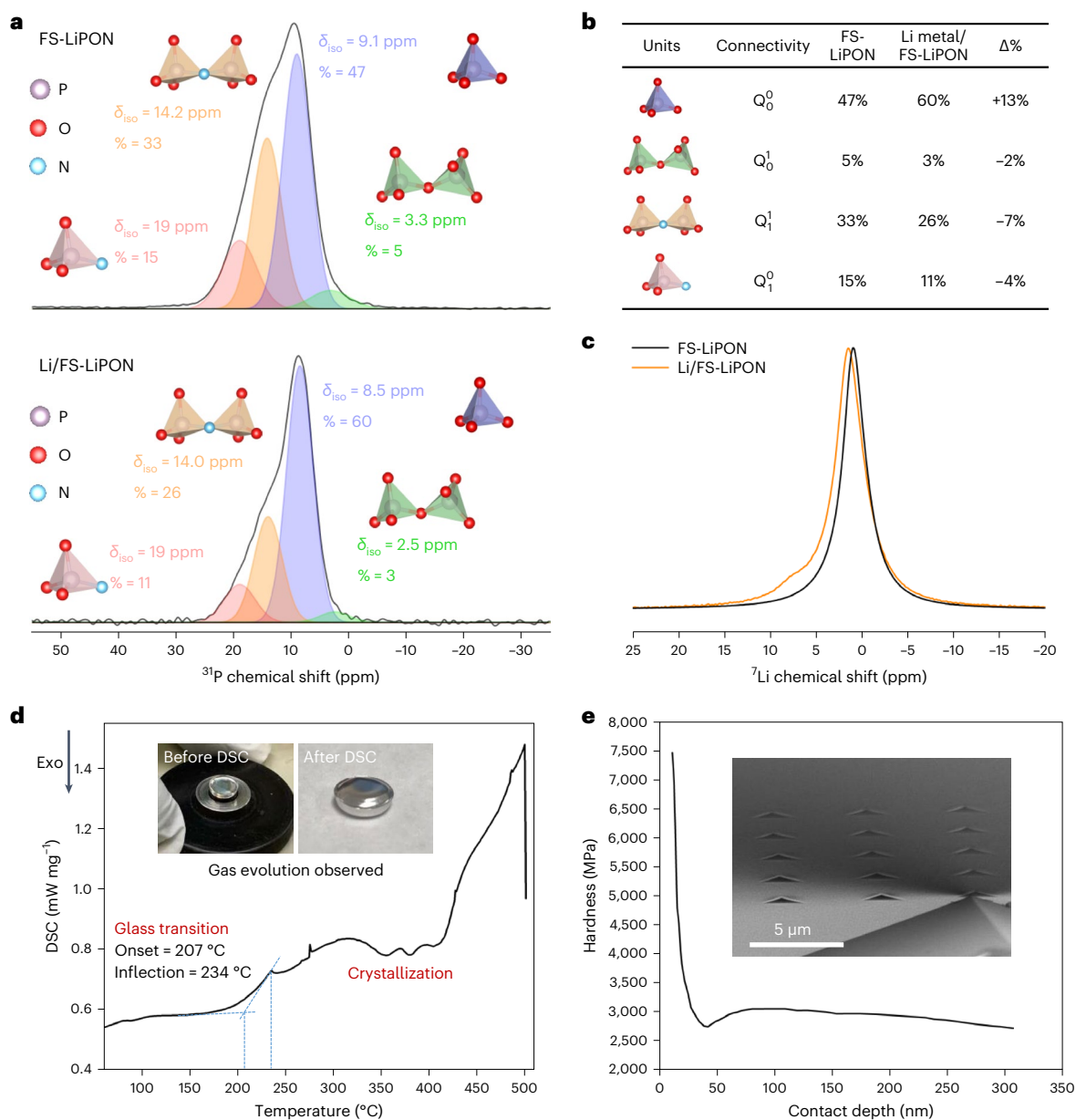


Fig. 2 | Interfacial chemistry, thermal properties and mechanical properties of FS-LiPON. **a**, ^{31}P MAS NMR spectra of the FS-LiPON and Li/FS-LiPON films. The spectrum of FS-LiPON is taken from our previous work²⁴ and used here for comparison. **b**, Structural unit component differences based on NMR deconvolution. Q_0^0 , orthophosphate tetrahedra PO_4^{3-} units; Q_1^0 , bridging-oxygen $\text{P}_2\text{O}_7^{4-}$ dimer units; Q_1^1 , bridging-nitrogen $\text{P}_2\text{O}_6\text{N}^{5-}$ dimer units; Q_1^0 , apical-nitrogen

PO_3N^{4-} units. **c**, ^7Li MAS NMR spectra of FS-LiPON and Li/FS-LiPON. **d**, DSC analysis of the FS-LiPON film. Inset: photographs showing the gas evolution due to DSC measurement. **e**, Film hardness values measured via CSM indentation up to $\sim 10\%$ of the film thickness. Inset: image showing the indent array on FS-LiPON during the nanoindentation experiment using a Berkovich indenter.

fabrication, the cell was tested using the configuration in Supplementary Fig. 1. Figure 3d shows the voltage curve of the Li-Cu cell during constant-current measurement. When a current of -50 nA is applied, the cell exhibits a voltage dip and reaches an overpotential of -1 V , after which a stable plating process proceeds. When altering the current direction, a stripping curve feature is obtained. The cell demonstrated a stable plating and stripping over 13 cycles without short-circuiting, indicating the ability of FS-LiPON to shuttle lithium ions. The relatively high overpotential is probably caused by the resistance to deformation of the copper current collector while lithium metal nucleates and grows. Apart from the nucleation barrier of lithium metal, extra mechanical work is needed to overcome the copper deformation. It is noteworthy that due to the unique configuration

of the FS-LiPON Li-Cu cell, no external pressure was applied to the cycled cell.

The plated lithium metal morphology in the FS-LiPON system was then examined by cryogenic focused ion beam/scanning electron microscopy (cryo-FIB/SEM). Figure 3e displays the cross-section morphology of the pristine Li-Cu cell, where no extra layer is observed between copper and the FS-LiPON before plating, and the evaporated lithium metal on the other side of the FS-LiPON appears fully dense. Note that cryogenic protection during FIB milling is crucial to preserve the pristine morphology and chemistry of lithium metal, as reported elsewhere previously³² and demonstrated in Supplementary Fig. 2. After a constant current plating, the Li-Cu cell shows a dense lithium layer with a dark contrast between copper and FS-LiPON in Fig. 3f.

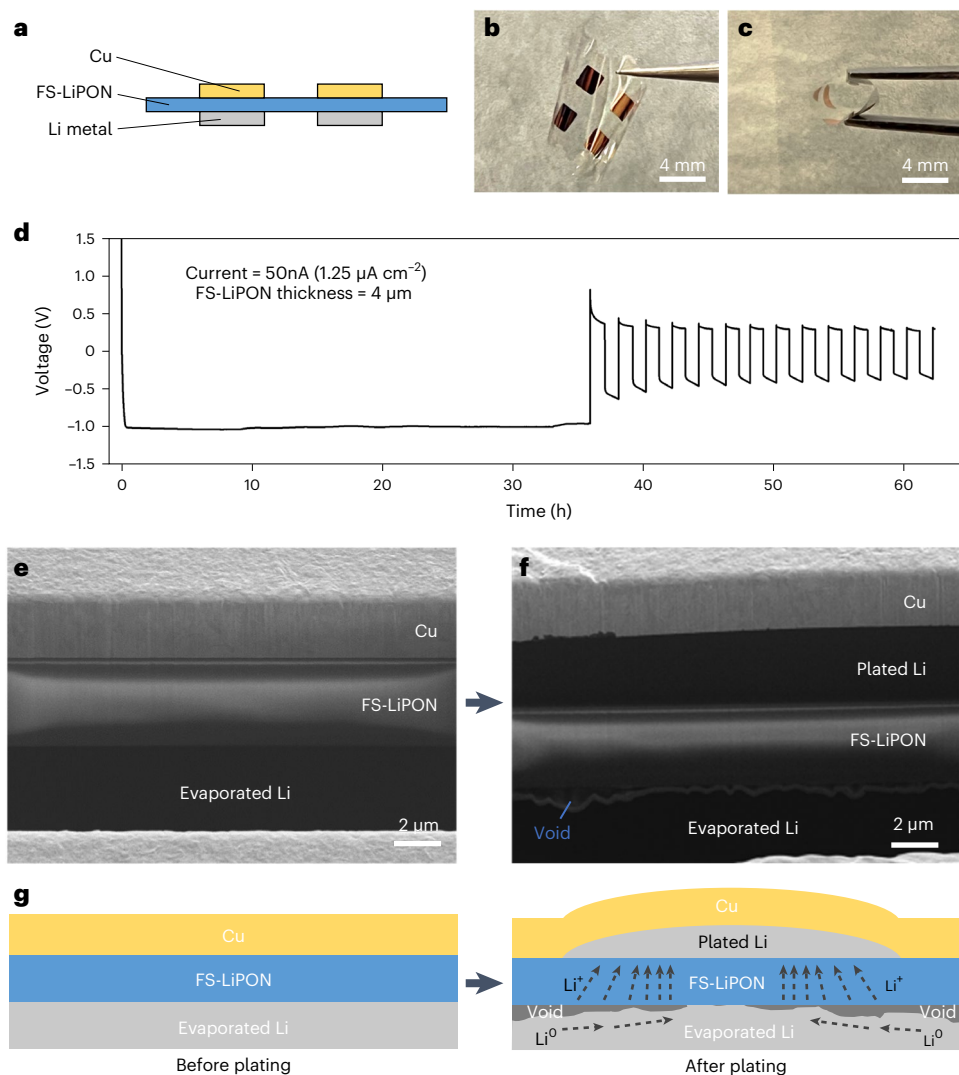


Fig. 3 | Electrochemical deposition and analysis on FS-LiPON. **a**, Cross-section schematic of the FS-LiPON Li-Cu cell. **b,c**, Photographs of the FS-LiPON Li-Cu cell from top view (**b**) and upon bending (**c**). **d**, Voltage curve of lithium metal plating and stripping in an FS-LiPON Li-Cu cell. **e,f**, Cross-section cryo-FIB/SEM images

of the Li-Cu cell before lithium metal plating (**e**) and after lithium metal plating (**f**). The plated capacity in **f** is $-0.31 \text{ mAh cm}^{-2}$. **g**, Schematic showing the proposed non-uniform void formation mechanism during lithium metal plating.

The associated Li-Cu cell voltage curve is plotted in Supplementary Fig. 3. The EDS mapping of a plated Li-Cu cell in Supplementary Fig. 4 illustrates the presence of copper, phosphorus, oxygen and gallium over the corresponding regions. Such features indicate that a fully dense lithium metal electrochemical deposition was realized by this FS-LiPON configuration when no external pressure was present.

Intriguingly, in Supplementary Fig. 4 a void region was observed between FS-LiPON and evaporated lithium metal, as hinted by the aggregation of the gallium signal that is commonly caused by redeposition during FIB milling and is prevalently found at the bottom of void region after FIB milling⁷. A similar void feature is also observed in Fig. 3f, where a gap is present between FS-LiPON and evaporated lithium. Although the theoretical thickness of plated lithium metal is calculated to be $1.5 \mu\text{m}$ based on the areal capacity, the observed region shows a plated lithium metal thickness of $\sim 4 \mu\text{m}$ in Fig. 3f. The top-view SEM image in Supplementary Fig. 5 displays various bumps distributed over the copper surface after plating. Figure 3g delineates the plating process occurring in the Li-Cu cell without pressure control. Before plating, each constituent in the cell is distinguishable by the well-defined interfaces. After plating, plated lithium metal

forces up the copper layer around the initial nucleation site, while the non-uniform lithium-ion flux within FS-LiPON drives lithium atoms around the vicinity of the nucleation site to migrate and compensate the metallic lithium reservoir immediately under the nucleation site. Therefore, void regions are formed around the nucleation site after plating is completed.

Fully dense, uniform lithium deposition without external pressure

The electrochemically deposited lithium metal in other SSE systems (that is, $\text{Li}_7\text{La}_3\text{Zr}_2\text{O}_{12}$ and $\text{Li}_6\text{PS}_5\text{Cl}$, etc.) usually appears fully dense regardless of dendrite formation issues. This kind of morphology is probably due to the presence of external pressure on the order of several MPa^{33,34}. Analogous to the cases of other solid-electrolyte systems, fully dense lithium metal plating has also been demonstrated in the FS-LiPON system. Nevertheless, it is noteworthy that no external pressure is applied to the LiPON system, suggesting the possible presence of interfacial stress that could act as internal pressure to promote lithium metal yielding and facilitate subsequent dense lithium metal deposition. Previous work by Motoyama et al. proposed a model to simulate

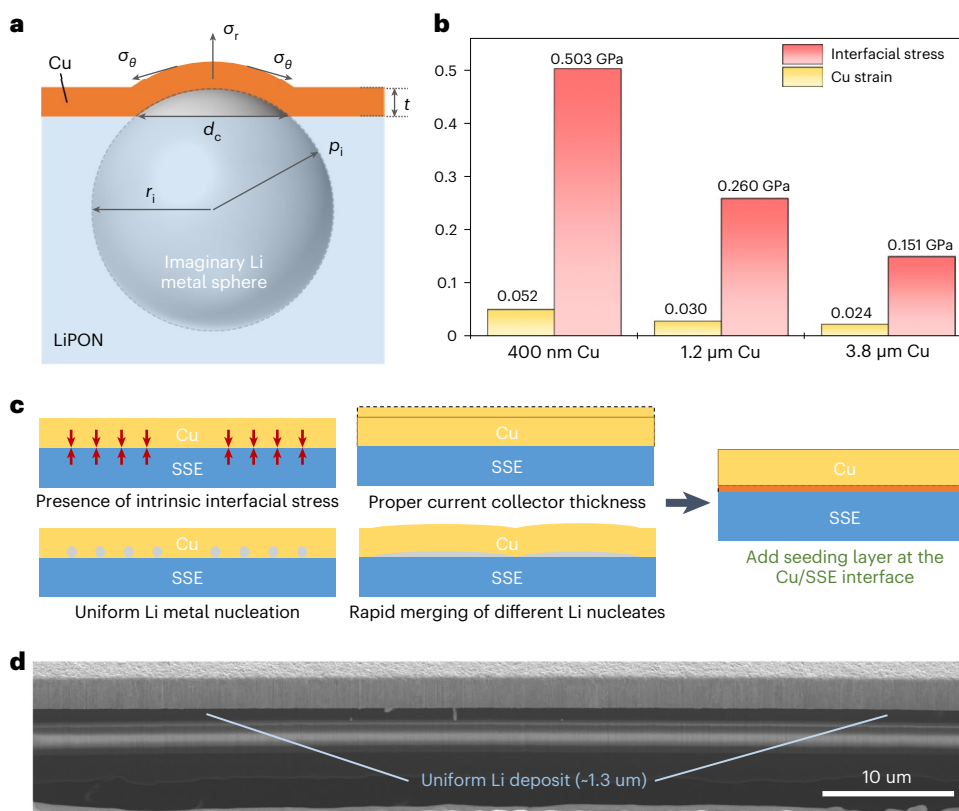


Fig. 4 | Stress analysis and proposed criteria for uniform lithium deposition.

a, Schematic of the interface model for interfacial stress simulation, where P_i is the interfacial stress between lithium and copper, σ_θ is the stress on copper in the circumferential directions, σ_r is the stress on copper in the radial direction, t is the thickness of copper, d_c is the length of the chord marked in the lithium sphere underneath the copper dome region, and r_i is the radius of the lithium

metal imaginary sphere. **b**, Copper strain and simulated interfacial stress in the Li–Cu cell for different copper thicknesses. **c**, Proposed principles and solution to achieve a uniform lithium metal deposition in a solid system. **d**, Cryo-FIB/SEM image showing uniform lithium deposition realized by adding a gold seeding layer in the FS-LiPON Li–Cu cell.

the interfacial stress between lithium metal and copper current collector after plating, where they used an imaginary lithium metal sphere and estimated the radial stress on the lithium metal surface based on the Hoop stress formula³⁵.

Employing the similar stress analysis model shown in Fig. 4a, we applied formula (1) as follows:

$$P_i = \frac{\varepsilon_{Cu} E_{Cu}}{(1 - \nu_{Cu})} \times \left\{ \frac{3(r_i + t)^3}{2[(r_i + t)^3 - r_i^3]} - \frac{\nu_{Cu}}{1 - \nu_{Cu}} \right\}^{-1} \quad (1)$$

where P_i is the interfacial stress between lithium and copper, ε_{Cu} is the strain in the circumferential directions, E_{Cu} is Young's modulus of copper, t is the thickness of copper, r_i is the radius of the lithium metal imaginary sphere, κ is the curvature of copper, and ν_{Cu} is the Poisson's ratio of copper. The input values of the above parameters were extracted from Supplementary Fig. 6 and are listed in Supplementary Fig. 7. Figure 4b shows the copper strain and resulting interfacial stresses in the Li–Cu cells with different copper thicknesses, ranging from 0.151 GPa to 0.503 GPa as the copper strain ramps from 0.024 to 0.052. The stresses obtained here are hundreds of times higher than the external pressure applied on bulk SSE analogues. Such high interfacial stress present at the copper–lithium interface confines the lithium metal morphology, thereby achieving a fully dense feature. Based on the stress formula given above, the interfacial stress is inversely proportional to the diameter of the lithium deposit and proportional to the copper strain, suggesting that lithium metal deposit tends to

have planary growth that can release overall stress, resulting in more uniform coverage of lithium metal on LiPON and less chance of dendrite formation. Therefore, we propose several criteria that need to be considered while building the ideal configuration for lithium metal plating in solid-state systems. As shown in Fig. 4c, intrinsic interfacial stress is essential to generate pressure during lithium metal plating without the aid of external pressure; proper current collector thickness is needed to confine lithium metal morphology while maintaining its own structural integrity; uniform lithium metal nucleation and rapid merging of different lithium nuclei help reduce the plastic deformation of the current collector to prolong cyclability. Consequently, one solution to achieve uniform lithium metal deposition is adding seeding layer at the copper–SSE interface to facilitate uniform lithium metal nucleation and subsequent uniform and dense lithium metal growth³⁶. Prior to depositing copper on FS-LiPON, a 3-nm-thick gold layer was first evaporated on FS-LiPON. The surface SEM image and EDS results in Supplementary Fig. 8 confirm the gold film formed on FS-LiPON before Li–Cu cell fabrication. After electrochemical plating without external pressure (Supplementary Fig. 9a), the copper surface remains relatively smooth as shown in Supplementary Fig. 9b, suggesting a uniform lithium metal deposition beneath. Figure 4d shows a cross-section image of the Li–Cu cell with the gold seeding layer after plating. The measured thickness of the lithium metal deposit is $-1.3 \mu\text{m}$, close to the thickness calculated from areal capacity (Supplementary Fig. 9a). The lithium metal deposit appears not only fully dense, but also uniform across the whole region. Small inclusions found in the plated lithium metal layer are probably, according to the cross-section

EDS in Supplementary Fig. 10, the Li–Au alloy. Based on above results, with the aid of interfacial stress and a seeding layer, uniform and fully dense lithium metal deposition can be realized in a solid-state system under zero external pressure.

Additionally, a further effort to demonstrate lithium stripping in the Li–Cu FS-LiPON cell is summarized in Supplementary Figs. 11 and 12. Although the Li–Cu FS-LiPON cell without external pressure ended up with non-uniform stripping that led to the formation of gaps between copper and FS-LiPON and generates inactive lithium (Supplementary Fig. 11), an external pressure of -87.5 kPa helped greatly improve the Coulombic efficiency to 82.7% (Supplementary Fig. 12). It is important to stress that external pressure appears to be essential for the stripping process, while uniformly dense lithium metal plating could be realized via just interfacial stress and a seeding layer. An intriguing observation was that the gap/void caused by stripping was formed between copper and lithium metal instead of being present between lithium metal and FS-LiPON (Supplementary Fig. 12), in contrast to the scenarios reported in bulk solid-state systems using argyrodite- or garnet-type SSEs^{37,38}. This difference is indeed related to the various current densities applied. Nevertheless, the fact that no void occurred between lithium metal and the SSE in this case might be related to LiPON's unique amorphous characteristic and its electrochemical stability against lithium metal.

Conclusions

This work presents a methodology to produce a thin-film LiPON in a free-standing form that is transparent and demonstrates remarkable flexibility. The absence of substrate enables fundamental studies of LiPON and the Li/LiPON interface by ss-NMR. DSC captures the glass-transition behaviour of LiPON around 207 °C with a high S/N ratio. Nanoindentation and flexibility testing yield a Young's modulus of ~ 33 GPa for LiPON and show the flexible nature of LiPON film, respectively. An electrochemical cell employing FS-LiPON shows its ability to conduct lithium ions. Stress analysis at the lithium–copper interface suggests the presence of a high compressive stress of the order of 10^{-1} GPa, which facilitates lithium metal yielding and a dendrite-free, dense lithium metal morphology. Using a gold seeding layer, we realize fully dense and uniform lithium metal deposition under zero external pressure. These conditions, combining interfacial stress and a seeding layer, are ideal for uniform lithium metal deposition. The amorphous nature and interfacial stability of LiPON prevents void formation within lithium metal deposits during the stripping process. We believe that this free-standing form of LiPON thin films will lead to a wider application of LiPON material. When coupled with cast cathodes, FS-LiPON can potentially enable lithium metal anode deposition with minimal external pressure.

Online content

Any methods, additional references, Nature Portfolio reporting summaries, source data, extended data, supplementary information, acknowledgements, peer review information; details of author contributions and competing interests; and statements of data and code availability are available at <https://doi.org/10.1038/s41565-023-01478-0>.

References

1. Yu, X., Bates, J. B., Jellison, G. E. & Hart, F. X. A stable thin-film lithium electrolyte: lithium phosphorus oxynitride. *J. Electrochem. Soc.* **144**, 524 (1997).
2. Bates, J. B. et al. Electrical properties of amorphous lithium electrolyte thin films. *Solid State Ion.* **29**, 42–44 (1992).
3. Lacivita, V. et al. Resolving the amorphous structure of lithium phosphorus oxynitride (LiPON). *J. Am. Chem. Soc.* **140**, 11029–11038 (2018).
4. Santhanagopalan, D. et al. Interface limited lithium transport in solid-state batteries. *J. Phys. Chem. Lett.* **5**, 298–303 (2014).
5. Wang, Z. et al. In situ STEM-EELS observation of nanoscale interfacial phenomena in all-solid-state batteries. *Nano Lett.* **16**, 3760–3767 (2016).
6. Wang, Z. et al. Effects of cathode electrolyte interfacial (CEI) layer on long term cycling of all-solid-state thin-film batteries. *J. Power Sources* **324**, 342–348 (2016).
7. Cheng, D. et al. Unveiling the stable nature of the solid electrolyte interphase between lithium metal and lipon via cryogenic electron microscopy. *Joule* **4**, 2484–2500 (2020).
8. Hood, Z. D. et al. Elucidating interfacial stability between lithium metal anode and Li phosphorus oxynitride via in situ electron microscopy. *Nano Lett.* **21**, 151–157 (2021).
9. Lewis, J. A., Tippens, J., Cortes, F. J. Q. & McDowell, M. T. Chemo-mechanical challenges in solid-state batteries. *Trends Chem.* <https://doi.org/10.1016/j.trechm.2019.06.013> (2019).
10. Herbert, E. G., Tenhaeff, W. E., Dudney, N. J. & Pharr, G. M. Mechanical characterization of LiPON films using nanoindentation. *Thin Solid Films* **520**, 413–418 (2011).
11. Xu, F. et al. Complete elastic characterization of lithium phosphorous oxynitride films using picosecond ultrasonics. *Thin Solid Films* **548**, 366–370 (2013).
12. Zhao, S., Fu, Z. & Qin, Q. A solid-state electrolyte lithium phosphorus oxynitride film prepared by pulsed laser deposition. *Thin Solid Films* **415**, 108–113 (2002).
13. Kozen, A. C., Pearse, A. J., Lin, C. F., Noked, M. & Rubloff, G. W. Atomic layer deposition of the solid electrolyte LiPON. *Chem. Mater.* **27**, 5324–5331 (2015).
14. Liu, W. Y., Fu, Z. W., Li, C. L. & Qin, Q. Z. Lithium phosphorus oxynitride thin film fabricated by a nitrogen plasma-assisted deposition of E-beam reaction evaporation. *Electrochem. Solid-State Lett.* **7**, 36–41 (2004).
15. Nowak, S., Berkemeier, F. & Schmitz, G. Ultra-thin LiPON films—fundamental properties and application in solid state thin film model batteries. *J. Power Sources* **275**, 144–150 (2015).
16. Kim, H. T., Mun, T., Park, C., Jin, S. W. & Park, H. Y. Characteristics of lithium phosphorous oxynitride thin films deposited by metal-organic chemical vapor deposition technique. *J. Power Sources* **244**, 641–645 (2013).
17. Muñoz, F. et al. Increased electrical conductivity of LiPON glasses produced by ammonolysis. *Solid State Ion.* **179**, 574–579 (2008).
18. Westover, A. S. et al. Plasma synthesis of spherical crystalline and amorphous electrolyte nanopowders for solid-state batteries. *ACS Appl. Mater. Interfaces* **12**, 11570–11578 (2020).
19. López-Aranguren, P. et al. Crystalline LiPON as a bulk-type solid electrolyte. *ACS Energy Lett.* <https://doi.org/10.1021/acsenergylett.0c02336> (2021).
20. Bates, J. B. et al. Fabrication and characterization of amorphous lithium electrolyte thin films and rechargeable thin-film batteries. *J. Power Sources* **43**, 103–110 (1993).
21. Schwöbel, A., Hausbrand, R. & Jaegermann, W. Interface reactions between LiPON and lithium studied by in-situ X-ray photoemission. *Solid State Ion.* **273**, 51–54 (2015).
22. Le Van-Jodin, L., Ducroquet, F., Sabary, F. & Chevalier, I. Dielectric properties, conductivity and Li⁺ ion motion in LiPON thin films. *Solid State Ion.* **253**, 151–156 (2013).
23. Li, J., Ma, C., Chi, M., Liang, C. & Dudney, N. J. Solid electrolyte: the key for high-voltage lithium batteries. *Adv. Energy Mater.* **5**, 1401408 (2015).
24. Marple, M. A. T. et al. Local structure of glassy lithium phosphorus oxynitride thin films: a combined experimental and ab initio approach. *Angew. Chem. Int. Ed.* **59**, 22185–22193 (2020).
25. Köcher, S. S. et al. Chemical shift reference scale for Li solid state NMR derived by first-principles DFT calculations. *J. Magn. Reson.* **297**, 33–41 (2018).

26. Vieira, E. et al. Flexible solid-state Ge–LiCoO₂ battery: from materials to device application. *Adv. Mater. Lett.* **8**, 820–829 (2017).
27. Sepúlveda, A., Criscuolo, F., Put, B. & Vereecken, P. M. Effect of high temperature LiPON electrolyte in all solid state batteries. *Solid State Ion.* **337**, 24–32 (2019).
28. Kalnaus, S., Westover, A. S., Kornbluth, M., Herbert, E. & Dudney, N. J. Resistance to fracture in the glassy solid electrolyte Lipon. *J. Mater. Res.* <https://doi.org/10.1557/s43578-020-00098-x> (2021).
29. Ma, D., Chung, W. O., Liu, J. & He, J. Determination of Young's modulus by nanoindentation. *Sci. China E* **47**, 398–408 (2004).
30. Abadias, G. & Daniel, R. in *Handbook of Modern Coating Technologies* (eds Aliofkhaeaei, M. et al.) 359–436 (Elsevier, 2021).
31. Swadener, J. G., Taljat, B. & Pharr, G. M. Measurement of residual stress by load and depth sensing indentation with spherical indenters. *J. Mater. Res.* **16**, 2091–2102 (2001).
32. Lee, J. Z. et al. Cryogenic focused ion beam characterization of lithium metal anodes. *ACS Energy Lett.* **4**, 489–493 (2019).
33. Wang, M. J., Carmona, E., Gupta, A., Albertus, P. & Sakamoto, J. Enabling 'lithium-free' manufacturing of pure lithium metal solid-state batteries through in situ plating. *Nat. Commun.* **11**, 5201 (2020).
34. Lee, Y. G. et al. High-energy long-cycling all-solid-state lithium metal batteries enabled by silver–carbon composite anodes. *Nat. Energy* **5**, 299–308 (2020).
35. Motoyama, M., Ejiri, M. & Iriyama, Y. Modeling the nucleation and growth of Li at metal current collector/LiPON interfaces. *J. Electrochem. Soc.* **162**, A7067–A7071 (2015).
36. Yan, K. et al. Selective deposition and stable encapsulation of lithium through heterogeneous seeded growth. *Nat. Energy* **1**, 16010 (2016).
37. Lee, K., Kazyak, E., Wang, M. J., Dasgupta, N. P. & Sakamoto, J. Analyzing void formation and rewetting of thin in situ-formed Li anodes on LLZO. *Joule* **6**, 2547–2565 (2022).
38. Kasemchainan, J. et al. Critical stripping current leads to dendrite formation on plating in lithium anode solid electrolyte cells. *Nat. Mater.* **18**, 1105–1111 (2019).

Publisher's note Springer Nature remains neutral with regard to jurisdictional claims in published maps and institutional affiliations.

Springer Nature or its licensor (e.g. a society or other partner) holds exclusive rights to this article under a publishing agreement with the author(s) or other rightsholder(s); author self-archiving of the accepted manuscript version of this article is solely governed by the terms of such publishing agreement and applicable law.

© The Author(s), under exclusive licence to Springer Nature Limited 2023

Methods

Photoresist spin coating

AZ1512 photoresist (EMD Performance Materials) is coated on clean glass substrate by spin coating. The heater temperature for prebake and postbake was set to 100 °C. The spinning sequence is 500 r.p.m. for 20 s, 1,000 r.p.m. for 20 s and 2,000 r.p.m. for 60 s. The resulting photoresist layer thickness is about 1.7 µm, and ultraviolet light treatment for -1 min is then performed.

Thin-film deposition

LiPON thin film was deposited on photoresist-coated glass substrate by RF sputtering using a crystalline Li₃PO₄ target (2 inches in diameter; Plasmaterials) in an ultrahigh-purity nitrogen atmosphere. The base pressure of the sputtering system was 3.0×10^{-6} torr. LiPON deposition used a power of 50 W and a nitrogen gas pressure of 15 mtorr. The as-deposited LiPON thin film was 3.7 µm thick with a growth rate of -0.46 \AA s^{-1} . The copper pads for EIS tests and current collection were deposited by thermal evaporation using copper pellets (from Kurt J. Lesker, 99.99% purity). The growth rate was 1 \AA s^{-1} . The lithium metal anode for the Li–Cu cell was deposited by thermal evaporation with a base pressure of 2.5×10^{-8} torr and a growth rate of $3\text{--}4 \text{ \AA s}^{-1}$. The gold seeding layer was deposited by thermal evaporation using gold pellets (from Kurt J. Lesker, 99.99% purity). The growth rate was 1.5 \AA s^{-1} .

X-ray diffraction

Powder crystal X-ray diffraction was carried out on a Bruker micro-focused rotating anode, with double-bounced focusing optics resulting in Cu K_{α1} and K_{α2} radiation ($\lambda_{\text{avg}} = 1.54178 \text{ \AA}$) focused on the sample. A sample of FS-LiPON was mounted onto a four-circle kappa-geometry goniometer with an APEX II charge-coupled device detector.

Microscopic morphology and chemical analysis

SEM was performed using an FEI Apreo microscope with an electron beam energy of 5 keV and an electron beam current of 0.1 nA. EDS was collected using an electron beam energy of 5 keV by Pathfinder EDS software from Thermo Scientific.

XPS

XPS was performed in an AXIS Supra spectrometer (Kratos Analytical). XPS spectra were collected using monochromatized Al K_α radiation ($h\nu = 1486.7 \text{ eV}$) under a base pressure of 10^{-9} torr. To avoid moisture and air exposure, a nitrogen-filled glovebox was directly connected to the XPS spectrometer. All XPS measurements were collected with a $300 \times 700 \text{ \mu m}^2$ spot size. Survey scans were performed with a step size of 1.0 eV, followed by a high-resolution scan with 0.1 eV resolution for the Li 1s, C 1s, O 1s, N 1s and P 2p regions. A 5 keV argon plasma etching source was used for surface etching with a pre-etching for 5 s, etching for 60 s and post-etching for 10 s. All spectra were calibrated with adventitious C 1s (284.6 eV) and analysed by CasaXPS software.

Electrochemical measurements

A Biologic SP-200 potentiostat was used to measure the EIS and d.c. polarization of FS-LiPON, and the electrochemical cycling of Li–Cu FS-LiPON cells. The frequency range for EIS was 3 MHz to 100 mHz with an amplitude of 10 mV and the obtained data were fitted with a linear least-squares fitting method. The constant voltage used for d.c. polarization was 1 V. The set-up for electrochemical measurement is shown in the schematic in Supplementary Figs. 6a and 10. To apply external pressure on Li–Cu FS-LiPON cell, a rigid stainless-steel plate ($2 \times 2 \times 0.03 \text{ mm}^2$) was placed between the active region of the cell and the probe during measurements.

ss-NMR

The NMR measurements performed on FS-LiPON and Li/FS-LiPON were collected using a 2.5 mm H/X/Y channel Bruker probe on a 600 MHz

Bruker Biospin Avance III, operating at 242.94 and 233.25 MHz for ³¹P and ⁷Li. The samples were packed within a 2.5 mm pencil-type ZrO₂ rotor and spun at 25 kHz. The ³¹P spectra were collected as a rotor-synchronized Hahn echo experiment with a 90° pulse of 2.54 µs (*B*₁ field strength, ~98 kHz). The Hahn echo experiments were processed from the top of the echo to remove the effects of ring down from the FID. A single pulse experiment with a pulse length of 2.875 µs (*B*₁ field strength, ~87 kHz) was used to acquire the ⁷Li spectra. The recycle delays used for the one-dimensional experiments were 60 s for ³¹P and 2 s for ⁷Li.

DSC

DSC measurements were conducted with a DSC 214 Polyma (Netzsch). The temperature range was from 50 °C to 500 °C with a heating rate of 10 °C min⁻¹. DSC measurements were conducted in a nitrogen environment. All samples were sealed in aluminium pans in an argon-filled glovebox to reduce contamination.

Nanoindentation

Nanoindentation was performed in a Thermo Fisher Scientific Scios 2 DualBeam FIB/SEM using a FemtoTools FT-NMT04 nanoindenter equipped with a Berkovich tip. Measurements of hardness and reduced modulus employed the CSM technique using a displacement-controlled test. Mechanical property values were averaged between displacements of -60 nm and -200 nm. Several five-by-five indent arrays were performed at various locations on the FS-LiPON films, which were bonded to SEM stubs with epoxy. Tests were performed using a 4 s load-ramp time and a 0.2 s unload-ramp time. When transferring samples from an inert environment to the Scios 2 SEM, samples were exposed to <120 s of atmosphere prior to the vacuum conditions inside the SEM.

Cryo-FIB/SEM

A FEI Scios DualBeam FIB/SEM equipped with cryo-stage was used to observe the surface and cross-section morphology of plated lithium metal in the FS-LiPON Li–Cu cell. The operating voltage of the electron beam was 5 kV. The emission current of the electron beam was set to 25 pA to minimize potential damage caused by the beam. A gallium ion beam source was used to mill and thin the sample. The operating voltage of the ion beam source was 30 kV. The emission currents of the ion beam were selected according to purpose: 10 pA for imaging by ion beam, 0.1 nA for cross-section cleaning and 3 nA for pattern milling. To preserve the lithium metal's pristine morphology, a cryo-stage was used during the pattern milling and cross-section cleaning processes, where the temperature of the cryo-stage was maintained at around -185 °C by heat exchange with cooled nitrogen gas.

Data availability

Additional data related to this paper are available from the corresponding authors upon reasonable request. Source data are provided with this paper.

Acknowledgements

We gratefully acknowledge funding support from the US Department of Energy, Office of Basic Energy Sciences, under award number DE-SC0002357. The FIB/SEM in this work was performed in part at the San Diego Nanotechnology Infrastructure (SDNI) of the University of California San Diego, a member of the National Nanotechnology Coordinated Infrastructure, which is supported by the National Science Foundation (grant ECCS-2025752). NMR was performed under the auspices of the US Department of Energy by Lawrence Livermore National Laboratory under contract number DE-AC52-07NA27344. XPS and DSC were performed at the UC Irvine Materials Research Institute (IMRI) using instrumentation funded in part by the

National Science Foundation Major Research Instrumentation Program under grant numbers CHE-1338173 and DMR-2011967.

Author contributions

D.C., M.Z. and Y.S.M. conceived the ideas. D.C., T.W., B.L., R.S. and B.S. prepared the thin-film samples. The FS-LiPON Li–Cu cell was designed by D.C. B.H., M.Z. and G.Z., and fabricated by D.C. M.M. performed and analysed ss-NMR measurements. D.C. conducted cryo-FIB/SEM and electrical measurements. D.C. and H.N. collected X-ray diffraction data. D.C., J.B. and P.H. collected and analysed the nanoindentation data. D.C., Y.Y. and W.L. collected XPS data. D.C., M.Z., Y.S.M., T.W., M.M., G.Z. and B.H. co-wrote the paper. All authors discussed the results and commented on the paper. All authors have approved the final paper.

Competing interests

The authors declare no competing interests.

Additional information

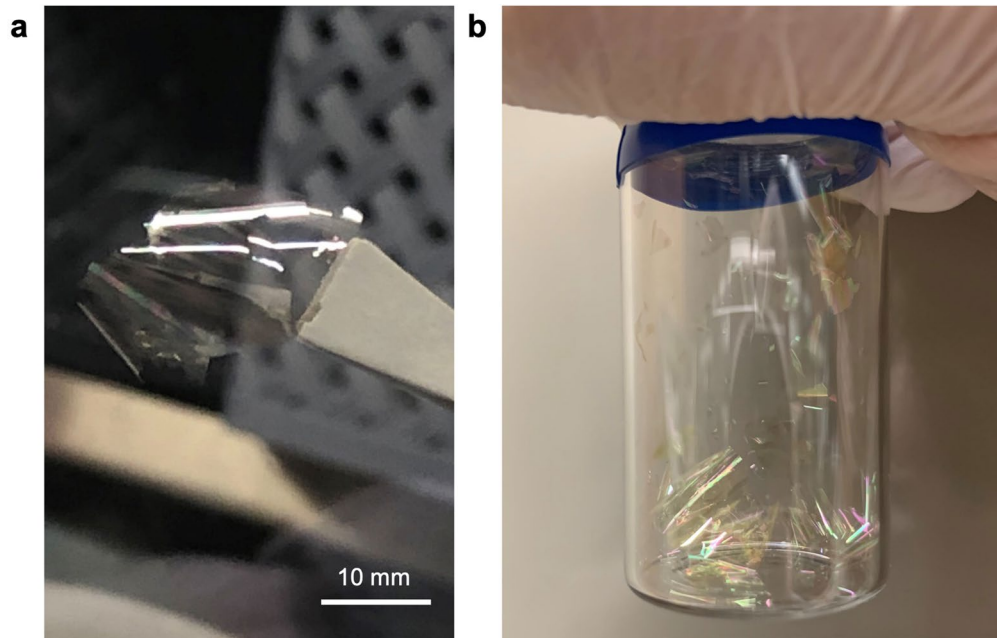
Extended data is available for this paper at <https://doi.org/10.1038/s41565-023-01478-0>.

Supplementary information The online version contains supplementary material available at <https://doi.org/10.1038/s41565-023-01478-0>.

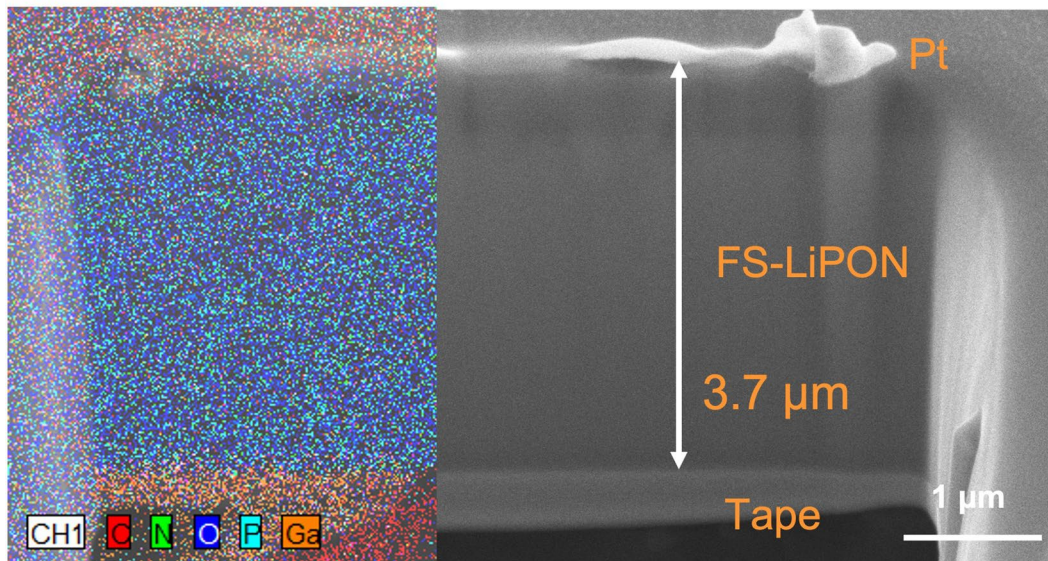
Correspondence and requests for materials should be addressed to Minghao Zhang or Ying Shirley Meng.

Peer review information *Nature Nanotechnology* thanks the anonymous reviewers for their contribution to the peer review of this work.

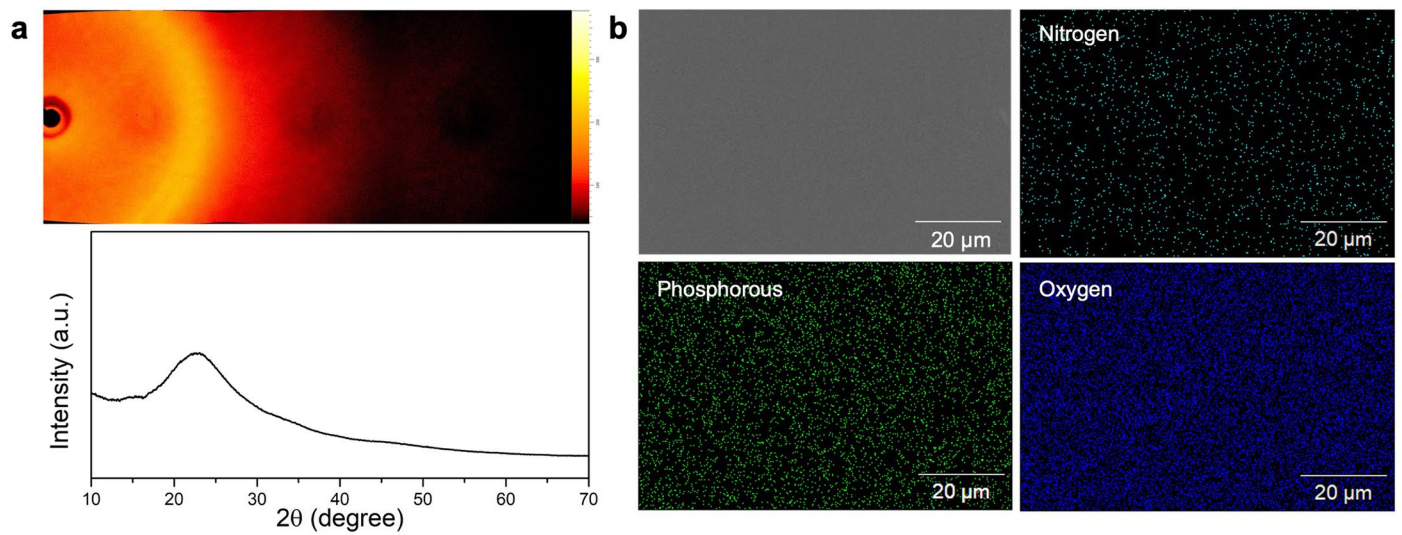
Reprints and permissions information is available at www.nature.com/reprints.



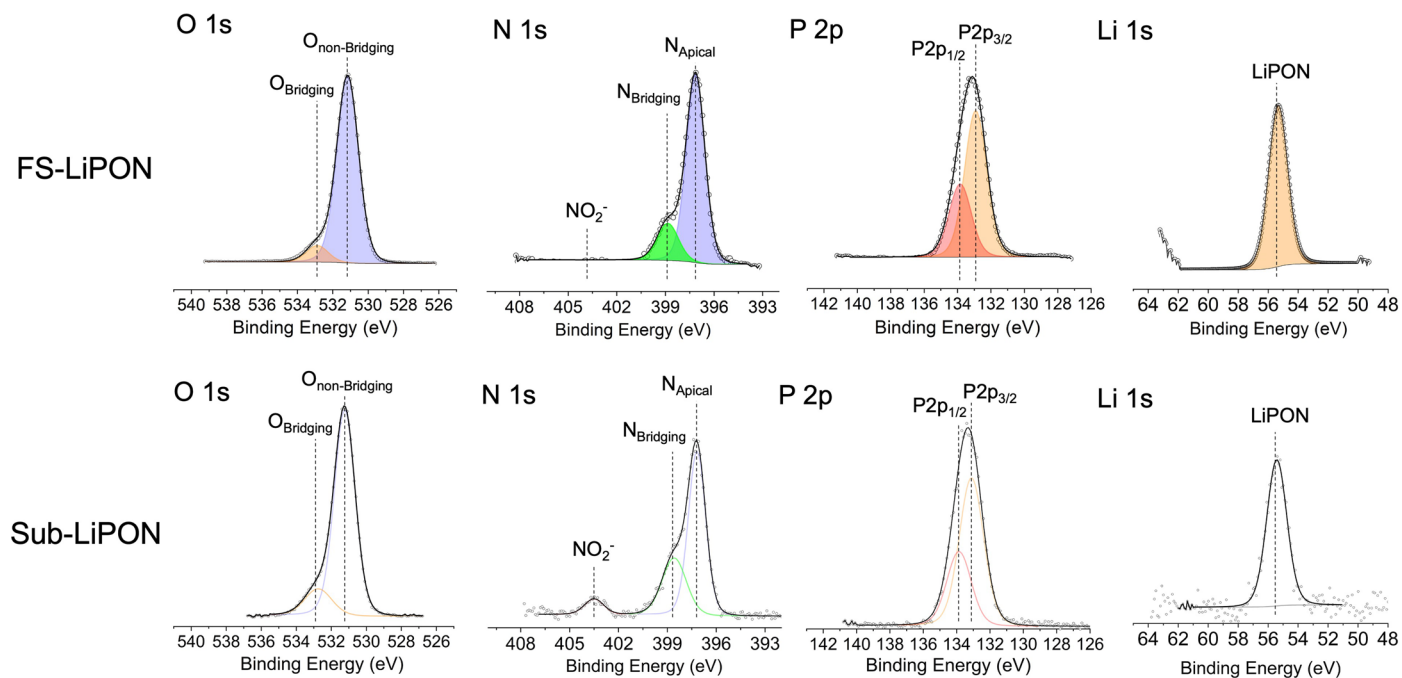
Extended Data Fig. 1 | Optical appearance of FS-LiPON film. a, Photo of a piece of transparent and flexible FS-LiPON film. **b,** FS-LiPON films with different sizes in a glass vial.



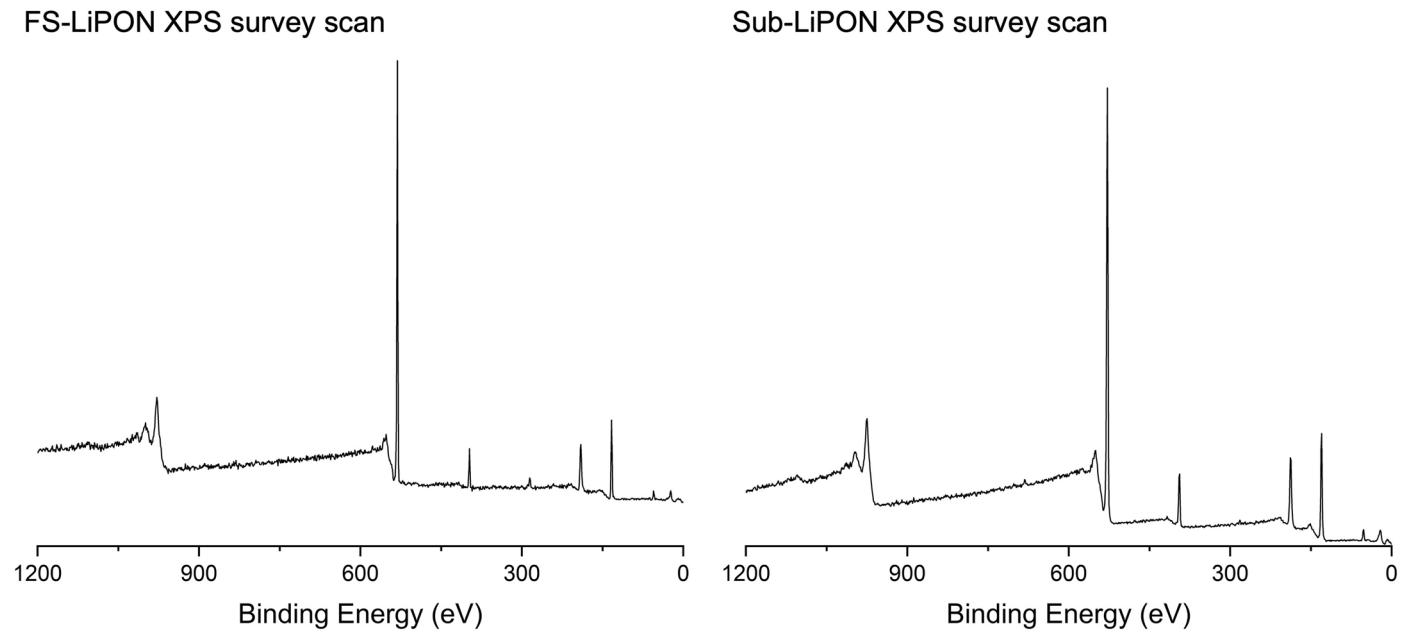
Extended Data Fig. 2 | Cross-section image of FS-LiPON with EDS mapping overlaid on the left part.



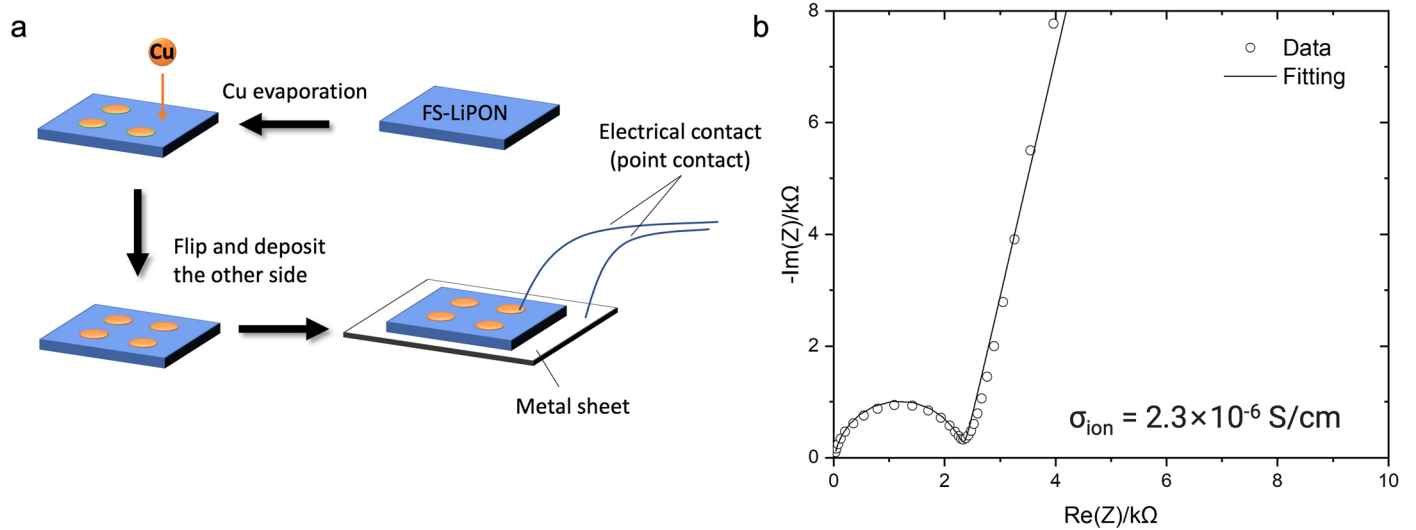
Extended Data Fig. 3 | XRD measurement and surface EDS mapping on FS-LiPON film. a, XRD pattern of FS-LiPON thin film. **b**, SEM image and EDS mapping on the surface of FS-LiPON.



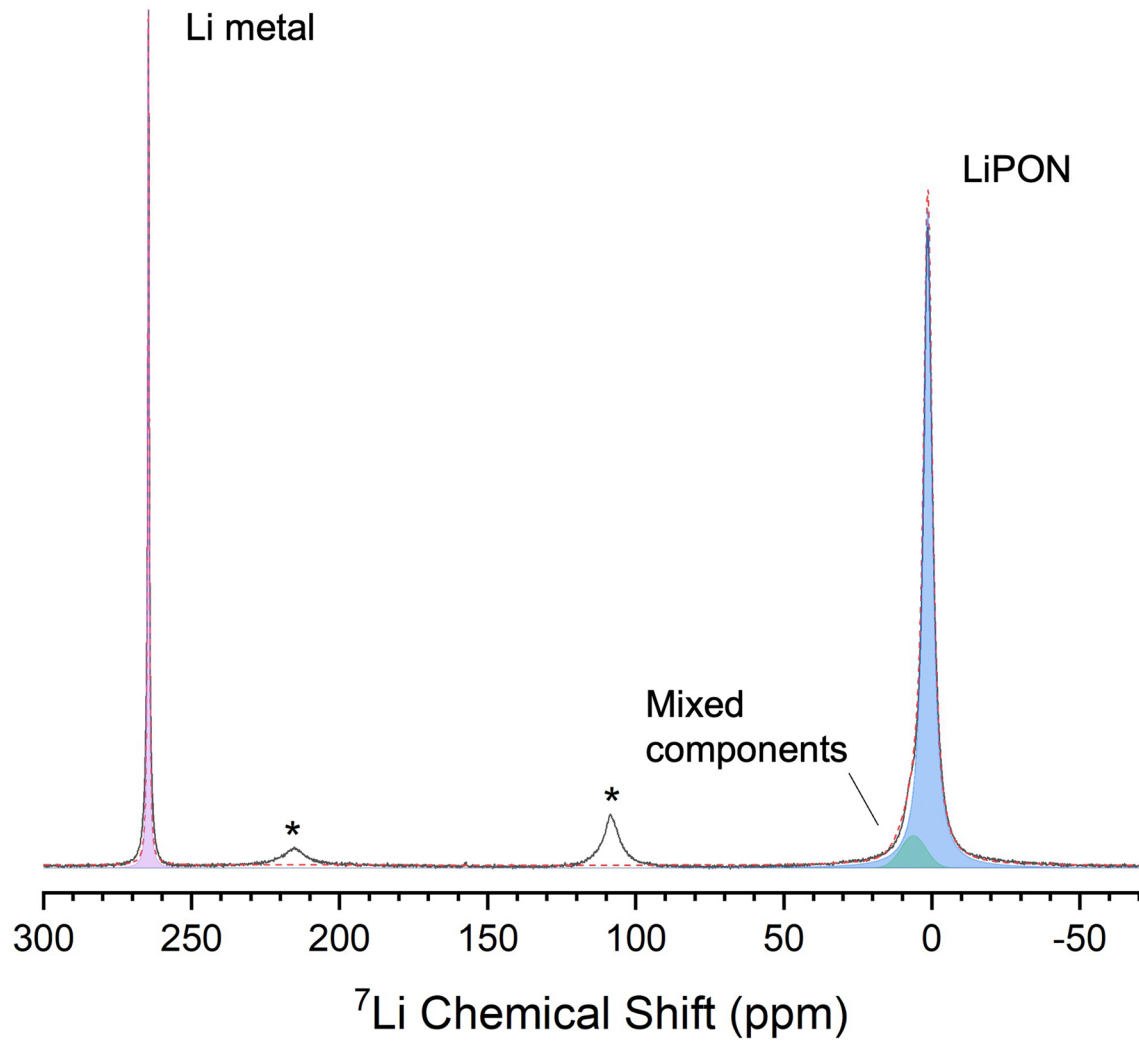
Extended Data Fig. 4 | XPS spectra of O 1s, N 1s, P 2p and Li 1s regions collected on FS-LiPON and sub-LiPON thin film. Note that the peak located at 403.5 eV in N 1s region of sub-LiPON can be attributed to NO_2^- species, which is not present in the FS-LiPON.



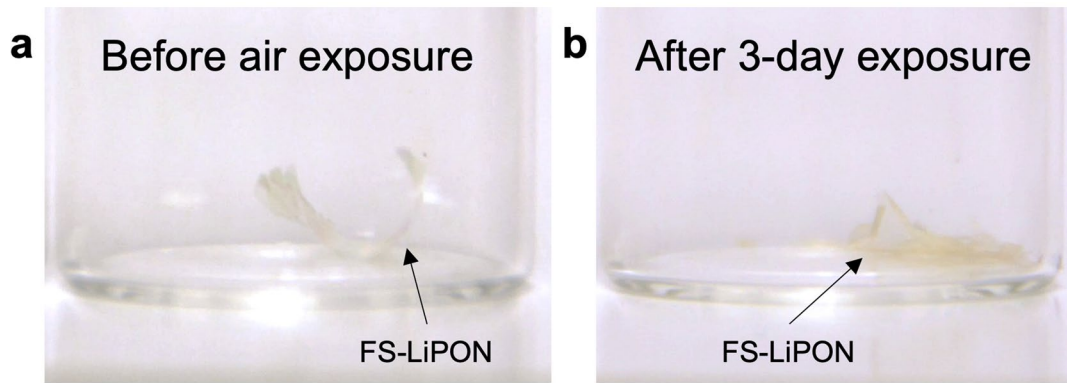
Extended Data Fig. 5 | XPS survey spectra of FS-LiPON and sub-LiPON films.



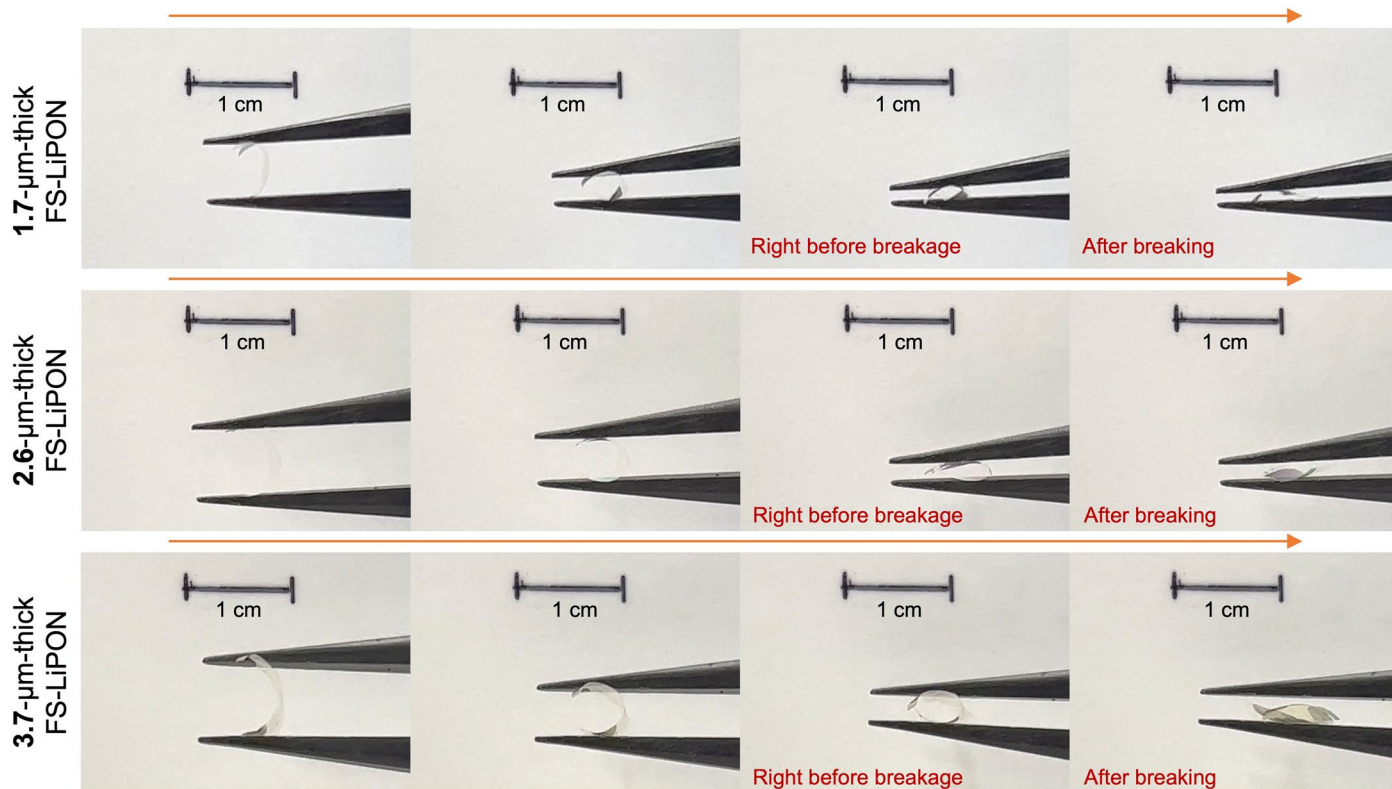
Extended Data Fig. 6 | EIS testing for FS-LiPON film. a, Testing configuration for the EIS measurement. **b**, EIS result collected on sub-LiPON.



Extended Data Fig. 7 | ${}^7\text{Li}$ MAS NMR spectrum of Li/FS-LiPON sample. The spectrum clearly shows the presence of Li metal in Li/FS-LiPON sample.



Extended Data Fig. 8 | Air exposure test on FS-LiPON film. Photos of the same piece of FS-LiPON film before air exposure (**a**) and after air exposure (**b**), showing the film shape change due to stiffening.



Extended Data Fig. 9 | Flexibility test on FS-LiPON film. Time-lapse series of images during the flexibility test on FS-LiPON films with thicknesses of 1.7 μm , 2.6 μm and 3.7 μm , respectively. A flathead tweezer was used to apply force on the FS-LiPON films whilst a video was taken to record the bending and

breakage of the film. As the time-lapse series of images show, all the FS-LiPON films exhibit remarkable flexibility upon bending. Right before film breakage, the 1.7- μm -thick film shows a high extent of bending compared with the 3.7- μm -thick film, indicating a higher flexibility.

Extended Data Table 1 | Existing methods for LiPON synthesis

| Synthesis method | Source/precursors | Substrate needed? | Ionic conductivity (25°C) | Notes |
|---|--|-------------------|---|--------------------------------------|
| Radio Frequency Sputtering ² | Li ₃ PO ₄ | Yes | 2.6×10 ⁻⁶ S/cm | |
| Pulsed Laser Deposition ¹³ | Li ₃ PO ₄ | Yes | 1.6×10 ⁻⁶ S/cm | Rough surface |
| Atomic Layer Deposition ¹⁴ | lithium tert-butoxide, H ₂ O, trimethylphosphate | Yes | 1.45×10 ⁻⁷ S/cm | Low growth rate |
| E-beam Evaporation ¹⁵ | Li ₃ PO ₄ | Yes | 6.0×10 ⁻⁷ S/cm | |
| Ion Beam Sputtering ¹⁶ | Li ₃ PO ₄ | Yes | 2.0×10 ⁻⁷ S/cm | Low growth rate |
| Metal-organic Chemical Vapor Deposition ¹⁷ | Li(C ₁₁ H ₁₉ O ₂), (C ₂ H ₅) ₃ PO ₄ | Yes | 2.95×10 ⁻⁷ S/cm | |
| Ammonolysis ¹⁸ | Li ₂ O·P ₂ O ₅ glass, NH ₃ | No | 10 ⁻⁷ ~10 ⁻⁹ S/cm | |
| Inductively Coupled Plasma ¹⁹ | Li ₂ O, Li ₄ P ₂ O ₇ , Li ₄ SiO ₄ , Si ₃ N ₄ | No | 1.0×10 ⁻⁶ S/cm | Low LiPON purity, in nanopowder form |
| Ball Milling ²⁰ | LiPO ₃ and Li ₃ N | No | 3.0×10 ⁻⁷ S/cm | Crystalline LiPON |